



## Article

# A VGGNet-Based Method for Refined Bathymetry from Satellite Altimetry to Reduce Errors

Xiaolun Chen <sup>1</sup>, Xiaowen Luo <sup>1,2,3,\*</sup>, Ziyin Wu <sup>1,2,4</sup>, Xiaoming Qin <sup>1,2</sup>, Jihong Shang <sup>1</sup>, Bin Li <sup>5</sup>, Mingwei Wang <sup>1</sup> and Hongyang Wan <sup>1</sup>

<sup>1</sup> Key Laboratory of Submarine Geosciences, Second Institute of Oceanography, Ministry of Natural Resources, 36 North Baochu Road, Hangzhou 310012, China

<sup>2</sup> Ocean College, Zhejiang University, 1 Zheda Road, Zhoushan 316021, China

<sup>3</sup> Key Laboratory of Ocean Space Resources Management Technology, Marine Academy of Zhejiang, 36 North Baochu Road, Hangzhou 310012, China

<sup>4</sup> School of Oceanography, Shanghai Jiao Tong University, 800 Dongchuan Road, Shanghai 200240, China

<sup>5</sup> National Center for Archaeology, 21 Building A, Zhuanjiaolou Nanli, Heping Street, Beijing 100013, China

\* Correspondence: luoxiaowen@sio.org.cn

**Abstract:** Only approximately 20% of the global seafloor topography has been finely modeled. The rest either lacks data or its data are not accurate enough to meet practical requirements. On the one hand, the satellite altimeter has the advantages of large-scale and real-time observation. Therefore, it is widely used to measure bathymetry, the core of seafloor topography. However, there is often room to improve its precision. Multibeam sonar bathymetry is more precise but generally limited to a smaller coverage, so it is in a complementary relationship with the satellite-derived bathymetry. To combine the advantages of satellite altimetry-derived and multibeam sonar-derived bathymetry, we apply deep learning to perform multibeam sonar-based bathymetry correction for satellite altimetry bathymetry data. Specifically, we modify a pretrained VGGNet neural network model to train on three sets of bathymetry data from the West Pacific, Southern Ocean, and East Pacific. Experiments show that the correlation of bathymetry data before and after correction can reach a high level, with the performance of  $R^2$  being as high as 0.81, and the normalized root-mean-square deviation (NRMSE) improved by over 19% compared with previous research. We then explore the relationship between  $R^2$  and water depth and conclude that it varies at different depths. Thus, the terrain specificity is a factor that affects the precision of the correction. Finally, we apply the difference in water depth before and after the correction for evaluation and find that our method can improve by more than 17% compared with previous research. The results show that the VGGNet model can perform better correction to the bathymetry data. Hence, we provide a novel method for accurate modeling of the seafloor topography.

**Keywords:** seafloor topography inversion; bathymetry; multibeam sonar; satellite altimetry; VGGNet



**Citation:** Chen, X.; Luo, X.; Wu, Z.; Qin, X.; Shang, J.; Li, B.; Wang, M.; Wan, H. A VGGNet-Based Method for Refined Bathymetry from Satellite Altimetry to Reduce Errors. *Remote Sens.* **2022**, *14*, 5939. <https://doi.org/10.3390/rs14235939>

Academic Editors: Baocheng Zhang and Teng Liu

Received: 16 October 2022

Accepted: 10 November 2022

Published: 24 November 2022

**Publisher's Note:** MDPI stays neutral with regard to jurisdictional claims in published maps and institutional affiliations.



**Copyright:** © 2022 by the authors. Licensee MDPI, Basel, Switzerland. This article is an open access article distributed under the terms and conditions of the Creative Commons Attribution (CC BY) license (<https://creativecommons.org/licenses/by/4.0/>).

## 1. Introduction

A seafloor topographic survey is a basic marine surveying and mapping technique to obtain seafloor topographic points' three-dimensional coordinates. This information includes measurement position, water depth, water level, sound speed, attitude, azimuth, and backscatter information, the core of which is water depth measurement.

Modern multibeam sounding systems began to rise in the 1960s. Fox et al. [1] conducted a quantitative analysis of the changes in the submarine topography caused by submarine volcanic eruption based on the multibeam sonar data and the submarine robot's measured images. Wu [2] put forward the critical statistical parameters to attain the seafloor tracking of the multi-beam sounding system and established the mathematical model and expert system for real-time monitoring of the seafloor terrain. Schimel et al. [3] analyzed

the continuous observation of multibeam data. They found that the uncertainty information provided by the multibeam processing algorithm CUBE can be used to calculate the displacement of the sediment volume better. Ma et al. [4] found that full coverage and high-efficiency multibeam sonar can be combined with side-scan sonar, which has good complementarity when detecting submarine targets and can improve the accuracy of target recognition. Ji [5] applied a backpropagation (BP) neural network to build a feature database of seabed terrain based on multibeam data to classify seabed terrain complexity automatically. Pike et al. [6] combined Pleiades' multispectral imagery and multibeam data to measure the water depth of two shallow areas in the northeastern Caribbean. Cooper et al. [7] proposed a method that uses small unmanned aerial vehicle (sUAV) photogrammetry and multibeam sonar data to generate a complete bathymetry map of a reservoir. Pydyn et al. [8] combined with a multibeam echosounder for underwater archaeological heritage sites to assist in the construction of a 3-D visualization model.

The multibeam sounding method has the advantage of high spatial precision, which enables the underwater sounding mode to achieve a high-quality leap from point to line and from line to surface [9]. However, with the low efficiency, high cost, and long measurement time required, these shortcomings make it difficult to conduct submarine surveys in a wide range of sea areas. Thus, the coverage of shipborne soundings is still very sparse at present. It is estimated that only less than 20% of the global sea area is covered with shipborne survey data, and a considerable part of it, especially in the deep ocean areas, consists of analog signals from 1950 to 1967, whose accuracy is relatively low [10].

There are several techniques for measuring water depth. Satellite imagery has been widely used to obtain optical multispectral image information over large surface areas. Airborne light detection and ranging (LiDAR) is capable of obtaining bathymetric information with only subpar accuracy to that of multibeam sonar. However, the electromagnetic beam of optical remote sensing tends to penetrate only to shallow water depths, making it difficult to operate over deeper waters [11,12]. Satellite altimetry is a space measurement technology that uses artificial satellites as a carrier to measure the distance of the satellite from the surface of the earth using radar, laser, and other ranging technologies. This method can obtain the surface terrain of our planet, through which a gravity field model and terrain features of the ocean can be constructed. Parker [13] derived the expression of gravity in the frequency domain and put forward the material interface of the model of abnormal gravity changes caused by fluctuations, which laid the foundation for the development of seafloor topography inversion. Since the launch of the Seasat in 1978, many researchers have used satellite altimetry data to model water depth, such as Dixon et al. [14], Smith and Sandwell [15], Ramillien and Cazenave [16], and Arabelos [17]. Calmant and Baudry [18] provided a comprehensive overview of the techniques and data used in bathymetric models. Yeu et al. [19] combined multibeam sonar, satellite altimetry-derived gravity anomalies, and airborne LiDAR data. They effectively improved the accuracy of water depth measurement for up to 0.2 m in shallow waters less than 5 m of depth. Brêda et al. [20] introduced and evaluated several data assimilation (DA) methods for satellite altimetry data, which have reduced the biased bathymetry errors in the hydrodynamic model by up to 65% compared to past observations while at the same time increasing the optimizer runtime to over 100 times. Wöfl et al. [21] summarized the significance, technology, data sources, development, and challenges of global seafloor topography surveys and research and proposed recommendations for the goal of a precise global bathymetry map inspired by the GEBCO Seabed 2030 Project. Sepúlveda et al. [22] established a sea depth uncertainty model for satellite altimetry, quantified the high-wavenumber content within the satellite-derived data, and proved the model in the bathymetry generated from the forecast of a tsunami, with specific parameters varying regionally.

The emergence of satellite altimetry has made seabed topography measurement no longer limited to shipborne sonar and has provided new technical means for large-scale, real-time global measurement. However, recent research has shown that compared with the multibeam-derived bathymetry, it still has the limitation on spatial resolution and

quality, influenced by parameters such as depth, surrounding topography environment, computational scales, orbits, and positioning signals [23–27].

In recent years, deep learning has become an essential scientific computing tool and made significant contributions and development in various aspects such as image classification [28–30], object detection [31], feature extraction [32], making multisource extensive data-based ocean observations available and efficient and consequently being applied to the field of seafloor topography inversion. Style transfer is a common method of photo artistry in popular culture, which, with the computation of neural networks, can abstract the style and content information of multiple photographs and fuse them into a new creation. The implementation of the idea was proposed and developed by Gatys et al. [33,34] and is able to obtain excellent results using the VGGNet framework, a convolutional neural network (CNN) widely used in visual recognition. Inspired by it, we can consider the multibeam sonar and satellite bathymetry data in this study as style information and content information, respectively, and extract both to blend them into a new image with both information, i.e., the corrected satellite bathymetry data.

Jena et al. [35] developed an artificial neural network (ANN) model based on the radial basis function (RBF) to predict the water depth based on satellite-derived gravity data. Their results demonstrated that the precision of the ANN model is higher than other submarine topography models. Jha et al. [36] used the direct geostatistical sampling (DS)-based multi-point statistics (MPS) algorithm, merging the low-frequency high-resolution multibeam sonar data and high-frequency low-coverage shipborne survey data, utilizing the former to provide prior constraining information to simulate and generate fine depth maps. Moran [37] discussed the global viability of machine learning models for inverting bathymetry and the probability of an enhanced global model by experiment and concluded machine learning could help determine a decision boundary when generating models. Ghorbanidehno et al. [38] introduced a principal component analysis (PCA)-connected deep neural network (DNN) to perform bathymetry inversion using flow velocity observations, proving its accuracy and availability for a high-dimensional riverbed topography model with sparse measurements.

By attaining the unification of the spatial resolution of multibeam data and the spatial coverage of satellite altimetry data, it can provide a new means for high-precision, real-time global seafloor topography surveying. This paper proposes a novel optimization algorithm based on VGGNet, a popular model for applying a convolutional neural network (CNN). In order to obtain a “content” and “style” representation of the data image, it is necessary to create some intermediate layers that represent the higher-order features of the image. The role of the intermediate layers is to match the corresponding style and content targets to the input image, converting the original image pixels into a complex understanding of the features present in the image in order to construct an internal representation. The Adam optimizer is used to minimize the loss. Instead of updating the weights associated with the network, the input images are trained by iterating to minimize the loss. This model enhances the precision of satellite altimetry-derived bathymetry by using the input of multibeam sonar bathymetry data. These datasets primarily lie in the range of the estimated average global ocean depth.

The main contributions of this article are as follows.

1. A combination of high-spatial-resolution multibeam sonar-derived bathymetry (truth data) and high-coverage satellite altimetry-derived bathymetry (to-be-corrected data). This information is synthesized to obtain a corrected version of the latter, with the advantage of both.
2. A convolutional neural network (CNN)-based VGGNet algorithm is for the first time proposed to compute the distance (loss) between the two inputs-to-be-corrected data and truth data, where the former is transformed by minimizing the distance between them with backpropagation, generating an image that best matches the latter.
3. Experiments are conducted in the West Pacific, Southern Ocean, and East Pacific, to test the algorithm’s performance, with the results showing that the improvement in

computational precision can reach over 17% compared with previous research as far as we conclude.

## 2. Methodology and Data

In this section, we elaborate on the related background of the CNN-based VGGNet (VGG-19) algorithm and its detailed application to the correction of the bathymetry data. As shown in Figure 1, the structure of the proposed network consists of mainly three parts: (1) the input of the truth and to-be-corrected bathymetry data; (2) the designation of the network model, requiring a pre-trained VGG-19 framework, a loss function, gradient descent, and the optimization loop; (3) the output of the corrected version of satellite altimetry-derived bathymetry data.

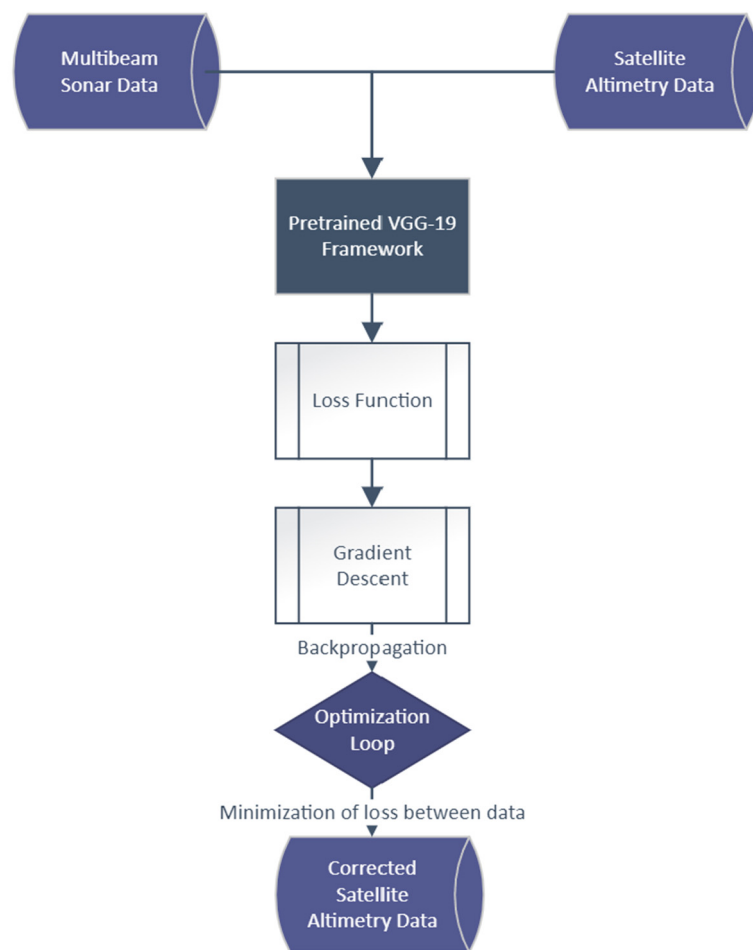


**Figure 1.** Main structure of the proposed network.

### 2.1. Framework of VGGNet

For the past decades, the convolutional neural network (CNN) models have been improved and updated for better application in large-scale image recognition, such as AlexNet [39], CaffeNet [40] and VGGNet [41], etc. VGGNet applies a very small field of perception instead of a large area field, using  $3 \times 3$  with a step size of 1. The decision function is more discriminative because there are 3 ReLU units. There are also fewer parameters, with 27 times the number of channels. Without modifying the perceptual field, VGGNet uses a  $1 \times 1$  convolutional layer to make the decision function more nonlinear. Due to the tiny size of the convolutional filter, the VGGNet model can have a considerable number of weight layers, which means better performance potential. There are two general forms of VGGNet, VGG-16 and VGG-19, which are not fundamentally different, but only differ in the depth of the network, with VGG-19 having three more convolution layers.

Considering the experimental requirements and data parameters, VGG-19, which can offer deeper information, is chosen in the experiment. Compared with most previous CNN-originated models that have 4–7 layers, VGG-19 is constructed with 19 layers, including 16 convolutional layers and 3 fully connected layers, enabling it to extract the more abstract and more profound image features and reduce the number of parameters while being able to retain the same receptive field. Thus, it has improved the efficiency and accuracy of image computing [42–44].

The structure of VGG-19 is displayed in Figure 2. The entire network uses the exact size of convolution kernels ( $3 \times 3$ ) and maximum pooling kernels ( $2 \times 2$ ). The combination of several small filter ( $3 \times 3$ ) convolutional layers is better than a large one ( $5 \times 5$  or  $7 \times 7$ ) as in the previous models. Since the convolution kernel focuses on expanding the number of channels and the pooling kernel focuses on reducing the width and height, the architecture is more profound and broader. At the same time, the increase in calculation slows down, showing the network a larger receptive field. At the same time, the network parameters are reduced, and the ReLU (Rectified Linear Unit) activation function is used multiple times to create more linear transformations to enhance the learning ability.

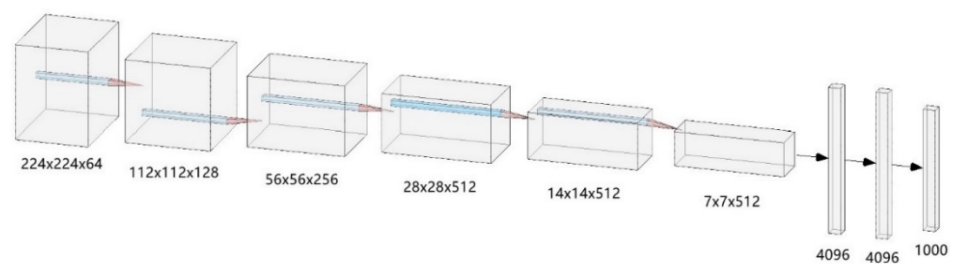


**Figure 2.** Architecture of the VGG-19 model. The boxes represent the size of each layer.

## 2.2. Model Training Steps

The correction of the bathymetry is conducted under the model of VGG-19. The overall framework is to take the satellite altimetric bathymetry data to be corrected as input values and the multibeam sonar bathymetry data to be treated as truth values as output. These procedures allow the machine to train a rationalization in the intermediate layer that minimizes the loss (distance) of this pair of datasets. The principle of the correction model is to define a distance function that describes how different the two input images are. The multibeam-derived data image and the satellite altimetry-derived data image covering the same area are passed to the model, which is supposed to return the intermediate layer outputs from the model. The distance function  $L$  that we use is shown below:

$$L^l(x, p) = \sum_{i,j} \left( F_{ij}^l(x) - P_{ij}^l(p) \right)^2 \quad (1)$$

where  $x$  stands for the multibeam sonar-derived bathymetry image,  $p$  stands for the satellite altimetry-derived bathymetry image, and  $i$  and  $j$  stand for the serial number of pixel points of the input images. Let  $V_{nn}$  be a pre-trained VGG-19 network and  $X$  be any image, then  $V_{nn}(X)$  is the network fed by  $X$ . Let  $F_{ij}^l(x) \in V_{nn}(x)$  and  $P_{ij}^l(p) \in V_{nn}(p)$  describe the respective intermediate feature representation of the network with the inputs  $x$  and  $p$  at layer  $l$ . At last, optimizers' rules are applied to iteratively update the images, which minimizes a given loss to the inputs.

The evaluation of the correction precision is based on comparisons with the previous study. To quantify the differences and connections between the predicted value and truth

value, here we choose two evaluation measurements, root-mean-square error (*RMSE*), normalized *RMSE* (*NRMSE*), and coefficient of determination ( $R^2$ ), as follows, respectively:

$$RMSE = \sqrt{\frac{\sum_{i=1}^n (\hat{f}_i - y_i)^2}{n}} \quad (2)$$

$$NRMSE = \frac{RMSE}{y_{max} - y_{min}} \quad (3)$$

$$R^2 = 1 - \frac{\sum_{i=1}^n (y_i - \hat{f}_i)^2}{\sum_{i=1}^n (y_i - \bar{y})^2} \quad (4)$$

where  $n$  represents the number of the values from the dataset,  $i$  represents the serial number of the value from the dataset,  $f$  represents the predicted values, and  $y$  represents the truth values. The normalization of *RMSE* can make datasets of different numerical ranges easier to compare. *NRMSE* and  $R^2$  usually range from 0 to 1. The smaller *RMSE*, *NRMSE*, and the bigger  $R^2$  mean that there is a higher correlation between the datasets.

Using the multibeam-derived data as the content image to match, we input and transform the satellite altimetry-derived data under the framework of VGG-19 to minimize the losses and distances between them. As a result, we can attain improved bathymetry data that combine the advantages of both the advantage of the high spatial precision of multibeam data and the high spatial coverage of satellite data.

### 2.3. Experiment Data

The original shipborne multibeam sonar bathymetry data used in the experiment were acquired at NOAA National Geophysical Data Center [45]. The interpolation preprocessing on the raw data is carried out to output the gridded digital elevation model (DEM) data. Meanwhile, the satellite altimetry data used in the experiment were acquired and extracted from NGDC's ETOPO1 1 arc-minute global relief model, clipped with the same range as the multibeam sonar data above [46]. The grid resampling of the satellite altimetry data is performed according to the resolution of the corresponding multibeam data to unify the pairs to facilitate subsequent operations.

We used three pairs of multibeam-satellite bathymetry data from the West Pacific, Southern Ocean, and East Pacific and conducted experimental analysis. The location and parameters of the data are shown in Figure 3 and Table 1. In particular, the acquisition time of the bathymetric data is not listed in the table because the seafloor topography does not develop perceptibly on a scale of decades without anthropogenic influence.

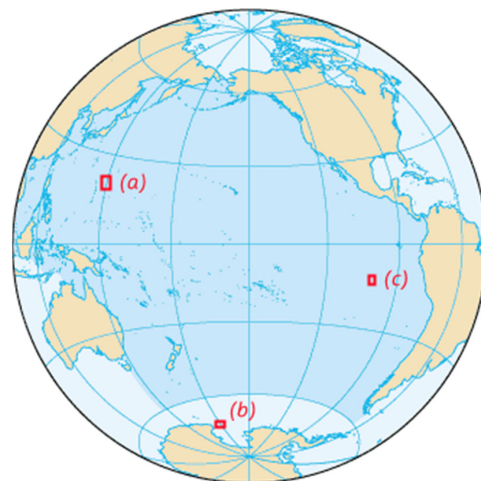


**Figure 3.** Location of the acquired bathymetry data in (a) West Pacific, (b) Southern Ocean, and (c) East Pacific.

**Table 1.** The parameters of the acquired bathymetry data.

	Coordinates of Center Point	Grid Resolution (m)	Data Size	Area (km <sup>2</sup> )	Depth Range (m)
West Pacific	19°N, 144°E	103	12,624,868	133,937	−8987—−369
Southern Ocean	71°S, 173°E	93	5,097,104	43,700	−4077—−211
East Pacific	27°S, 109°W	93	9,135,007	78,318	−3921—−1266

For the VGG-19 model, the input parameter is a pair of multibeam-satellite bathymetry data. The output parameter is the corrected satellite altimetry data. In the dataset, 50% are randomly selected as the training set to initially fit the model and update the parameters. The remaining 50% are created as the validation set to provide an unbiased evaluation of the model conducted on the training set, which is the prediction results.

### 3. Analysis of Results

The output of the model is the corrected satellite altimetry bathymetry data, as shown in Figure 4. As seen in the comparison, the overall texture of the bathymetric map becomes refined after correction, compared with the roughness of the original data, being closer to the real topographic pattern of the seafloor. It visually shows the effect of the correction model.

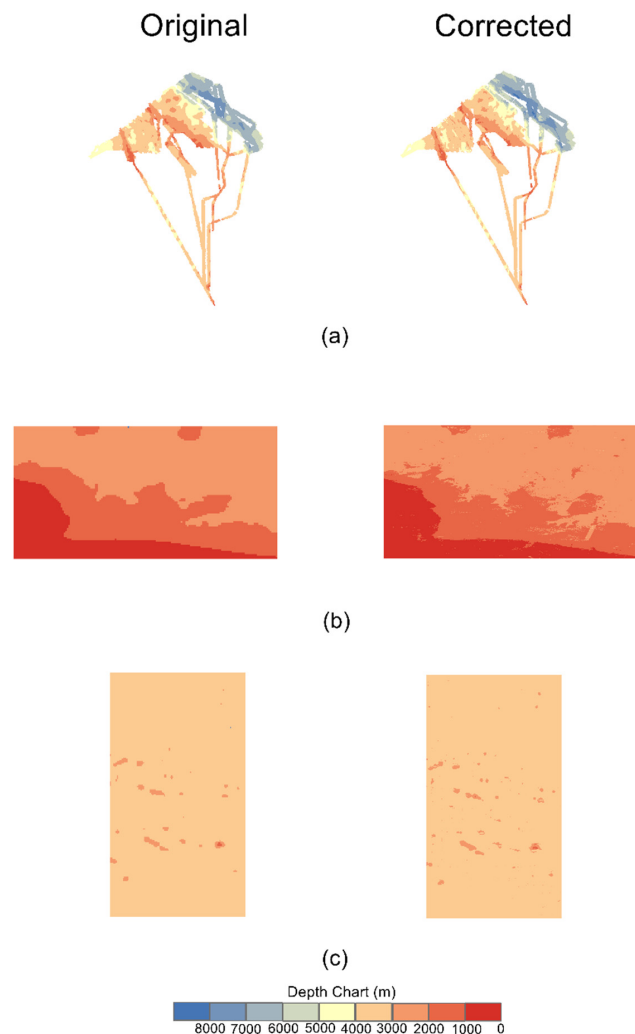


**Figure 4.** Bathymetric maps of (a) West Pacific, (b) Southern Ocean, and (c) East Pacific before and after correction.

The default hyperparameter settings of the VGG-19 model used for the experiments are listed in Table 2. The content layer, style layer, and the weights between content, style, and total variance loss were set so that they remained approximately the same order of magnitude in the experiments. The learning rate was set so that the iterations were performed in a convergent process and the loss curve decreases smoothly.

**Table 2.** Default hyperparameter settings of the model.

Hyperparameters	Settings
Content layer	'conv4_2'
Style layers	'conv1_1', 'conv2_1', 'conv3_1', 'conv4_1', 'conv5_1'
Weights of loss at content layer	1
Weights of loss at style layers	1, 1, 1, 1
Weights among content, style, and total variation loss	$1 \times 10^{-4}$ , $1$ , $1 \times 10^{-5}$
Learning rate	starts at 10, linear decay over 100 iterations to 1

The loss function is applied to estimate the gap between the output value of the model and the truth value to guide the subsequent optimization steps of the model. The smaller the loss function value, the better the model. The loss of the training and test sets is shown in Figure 5. In all the experimental areas, the loss of the model dropped sharply to around 0.2 after 20 epochs and started to decrease gradually, especially after 70 epochs. Moreover, it shows that no apparent overfitting phenomenon is found during the computing process. It can be concluded that the VGG-19 model can effectively reduce the loss of experimental data from these three sea areas.

The parameters of the model's performance are evaluated by running tests on 50% of the multibeam sonar data from the validation set, with its outcome listed in Table 3. From the perspective of  $R^2$ , there is a high correlation between the corrected datasets from the West Pacific, Southern Ocean, and East Pacific, respectively 0.80, 0.81 and 0.77, and the truth datasets, indicating an excellent fit. Regarding the RMSE and NRMSE, the figures show that the model results in errors of 267 m, 102 m, and 87 m in the West Pacific, Southern Ocean, and East Pacific datasets, along with the NRMSE being 0.031, 0.026, and 0.033, respectively. Compared with previous similar studies [35,36], our model can improve the NRMSE of the datasets by more than 19%, proving its potential. In addition, we believe there is a consistent trend in the changes of  $R^2$  and the RMSE, with the correction effect of the data in the Southern Ocean being the best, followed by the West Pacific and then the East Pacific.

**Table 3.** The overall precision of the correction.

	$R^2$	RMSE (m)	NRMSE
West Pacific	0.80	267	0.031
Southern Ocean	0.81	102	0.026
East Pacific	0.77	87	0.033

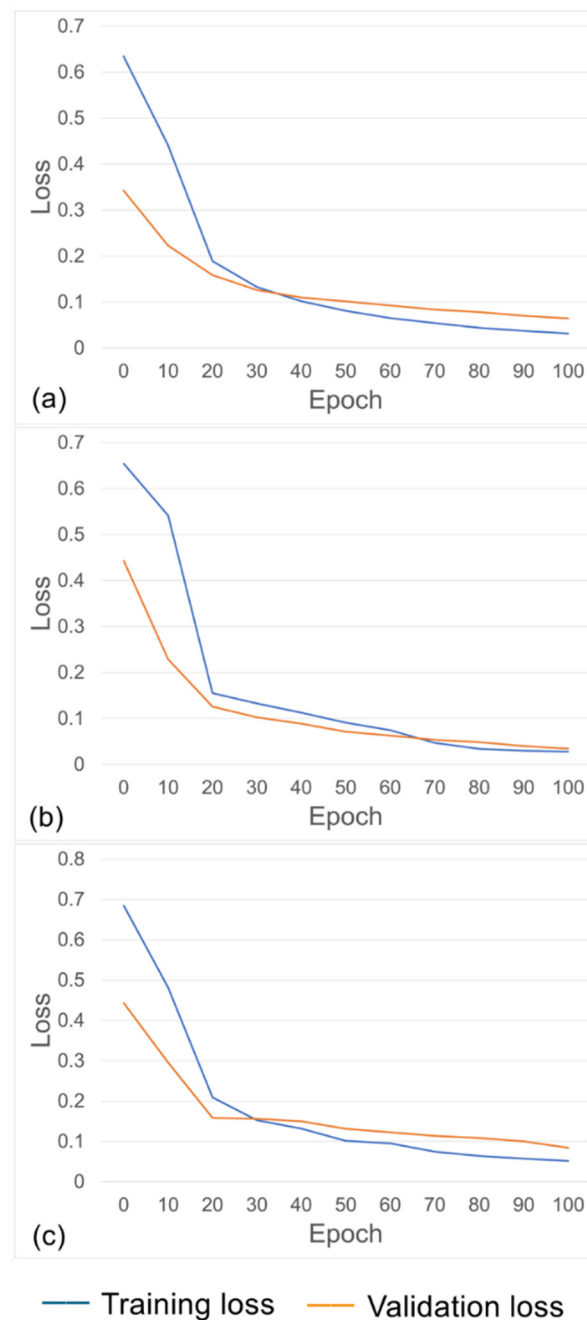


**Figure 5.** The loss of training set and validation set from the experiment of (a) West Pacific, (b) Southern Ocean and (c) East Pacific.

In the experiments, we find that the precision of the correction, taking  $R^2$  as an example, varies with the water depth, as shown in Figure 6. As can be seen from the figure, in general, the minimum  $R^2$  is above 0.2, which occurs at the extreme value of the water depth. At the same time, the maximum can reach more than 0.9, and the water depth in each water area varies, with maximum and minimum values for each sea area being almost identical. In the West Pacific data,  $R^2$  is higher than 0.8 in the water depth range from about  $-4500$  to  $-1900$  m, showing a strong correlation, with a maximum at about  $-3200$  m. For the Southern Ocean data,  $R^2$  is strongly correlated at around  $-500$  m and around  $-1800$  m to  $-2400$  m, with a maximum of around  $-2200$  m. For the East Pacific data,  $R^2$  is strongly correlated in the range from about  $-2400$  m to  $-3600$  m, with a maximum of about  $-3500$  m.

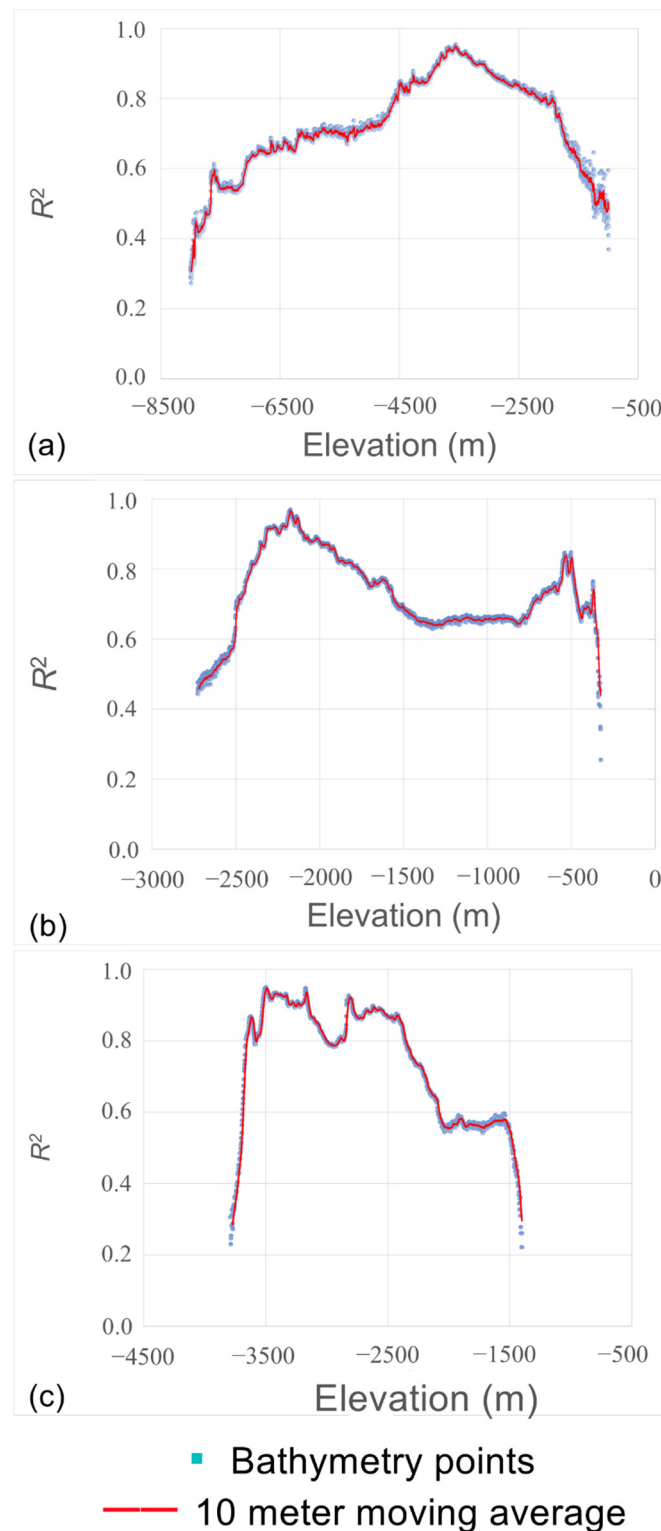


**Figure 6.** Relationship between water depth and precision ( $R^2$ ) in (a) West Pacific, (b) Southern Ocean, and (c) East Pacific.

From experience, the precision of machine learning is positively correlated with the data volume of the dataset samples. Without considering other parameters, the larger the sample size, the higher the learning precision, and vice versa. In the experiments, histograms of the distribution of water depth versus the number of data points were taken into account. In water depth ranges with significant variability in the number of data points,  $R^2$  shows a low level, whereas the depth ranges with high  $R^2$  tend to have a more

concentrated distribution and slighter variability. Specifically, the accuracy of the model is low in the case of smaller sample size, such as at the maximum and minimum values of water depth in these three experimental areas. In the depth range where the distribution sample size is large, the accuracy is reflective of high correlation. In general, the undulating variation of  $R^2$  at different water depths in the figure reflects the topographic specificity of the seafloor in the three areas. Experiments show that with the input of sufficient data volume, the satellite altimetry-derived bathymetry data corrected by the VGG-19 model can be highly fitted with the multibeam-derived data in specific water depth ranges.

Figure 7 illustrates the percentage distribution of the NRMSE (the original NRMSE values are expanded to 1000 times for ease of presentation). As mentioned before, like the RMSE, a smaller value of the NRMSE indicates higher accuracy, and vice versa. From the figure, it can be seen that the NRMSE distribution of the data in all three experiment regions roughly follows a pattern of high in the middle and low on both sides. That is, the percentage of data points with the highest and lowest precision are both small, and the percentage of those with the middle precision is the largest, and all lie in the range from 15% to 40%. The NRMSE values range from 0.018–0.036, 0.016–0.039 and 0.020–0.040 for the West Pacific, Southern Ocean and East Pacific, and the maximum percentages correspond to values of 0.021, 0.029 and 0.025, respectively. From the trend lines, both the West Pacific and East Pacific data exhibit smoother right-skewed distribution, indicating that the mean NRMSE for these two datasets is greater than the median and mode. The Southern Ocean data, on the other hand, are not significantly skewed, with two peaks around 0.018 and 0.029 and the rest relatively evenly distributed. Combined with Table 3, the Southern Ocean data have the best overall NRMSE performance, and it can be assumed that the relative average trend of the Southern Ocean data curve still represents the best performance even though there are no peaks as prominent as the other two. The overall performance of the West Pacific data is better than that of the East Pacific, which can also be seen in the trend line of the two, i.e., with 0.023 as the dividing line, the percentage of the West Pacific data points is higher than that of the East Pacific when the NRMSE decreases, and vice versa.

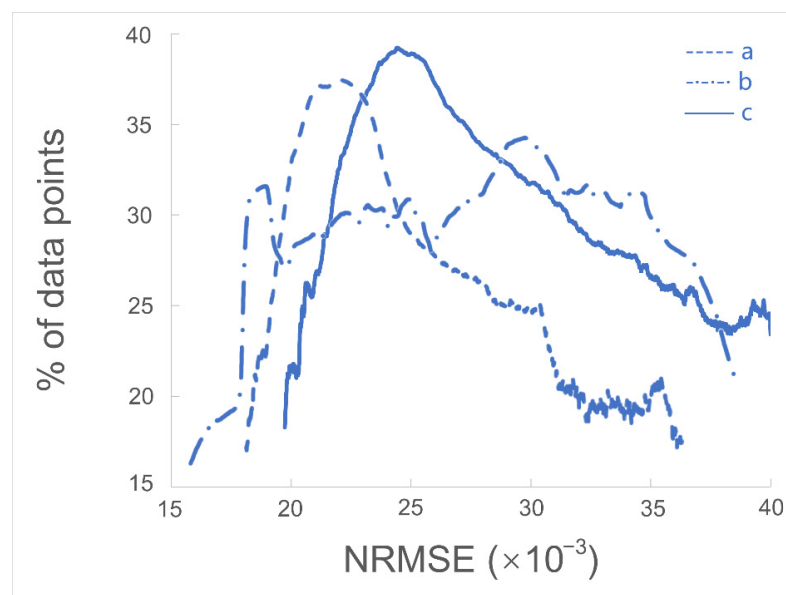
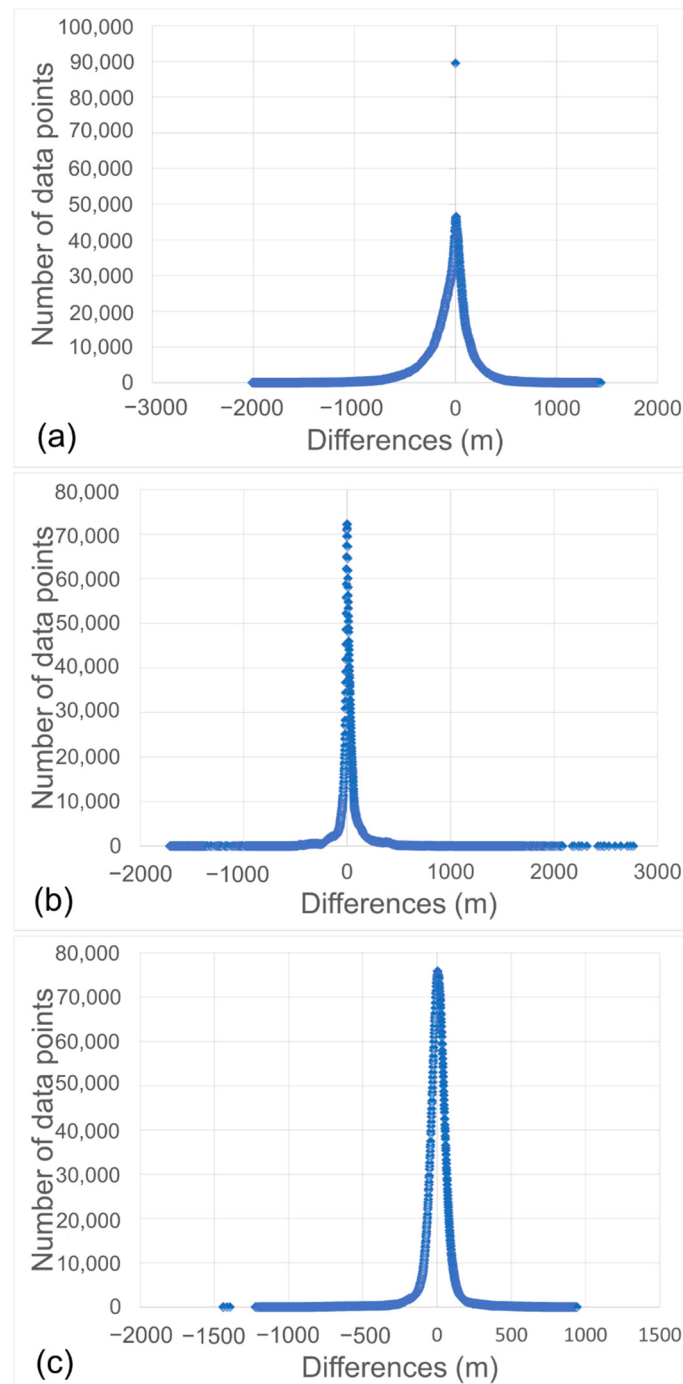


**Figure 7.** Percentage distributions of NRMSE ( $\times 10^{-3}$ ) in (a) West Pacific, (b) Southern Ocean, and (c) East Pacific.

We subtract the corrected water depth values of the satellite altimetry data from the truth value of the multibeam sonar data and then find that the distribution of errors between the two is in the form of high in the middle (zero) and low on both sides, that is, the closer the error is to 0, the greater the number of data points is, and vice versa, as

shown in Figure 8. In the West Pacific data, the data point with zero error as the maximum value is isolated, not continuous with the rest of the curve, indicating that the VGGNet model results in significantly more error-free bathymetry points. In the other two data, the data curves are relatively continuous, decreasing from the maximum value of zero to both sides. In contrast, the Southern Ocean data curve is more convergent near zero than the East Pacific one, indicating that its correction effect is better.



### ■ Bathymetry points

**Figure 8.** Differences between corrected and truth values in (a) West Pacific, (b) Southern Ocean, and (c) East Pacific.

For a more intuitive representation, we use the absolute value of the results above to calculate the percentage of the data within the range between 2% and 1% to the total depth of each data, with the values representing the errors from the truth value, as listed in Table 4. As the error range decreases, the number of data points increases gradually.

**Table 4.** Proportion of corrected errors from truth values within 2% and 1% depth range.

	2% of Depth (%)	1% of Depth (%)
West Pacific	67.25	45.73
Southern Ocean	76.19	60.34
East Pacific	68.30	41.55

On average, the data points with an error within 2% of the depth value account for 70.58% of the total and 49.21% within the 1% range. Compared with previous studies, the correction precision of the deep learning VGG-19 model can be effectively improved by over 17% [35,36].

Among the depth range indicators, the accuracy of the corrected Southern Ocean data is consistently better than the other two by a relatively large margin. In the 2% range, the East Pacific and West Pacific data performed almost indistinguishably, with the East Pacific data slightly higher. Combining that data with the information in Table 3, we find that the parameters show relative consistency. For most cases, the data of the Southern Ocean have the best correction, while the West Pacific and East Pacific data are the second and lowest, respectively.

#### 4. Conclusions

This study proposes a pretrained convolutional neural network (CNN)-based VGGNet deep learning model to correct the satellite bathymetry data. The core idea of the correction model is to define and minimize the distance (loss) between the truth data and to-be-corrected data, and finally output the corrected satellite altimetry seafloor topography accordingly. We then evaluate the model performance using three pairs of representative bathymetric datasets from the West Pacific, Southern Ocean, and East Pacific, respectively, with different hydrological environments and geographical locations. In the testing process, the loss of the training and validation set of the training process has been effectively reduced, proving the model's effectiveness.

We selected three indicators,  $R^2$ , RMSE, and its derived NRMSE, to evaluate the correction results of the data, showing excellent outcomes with the NRMSE indicator being over 19% higher than the previous research. Further, by analyzing the difference in  $R^2$  values at different water depths, we find that the correction precision of the deep learning model has a positive correlation trend with the sample size. That is, the accuracy of the depth values with more data points is higher, and vice versa.

Finally, we discover that the differences between the truth and corrected values gradually decrease from the maximum value at zero to both sides of the number axis. Then, we analyze the proportion of the absolute value of the difference to the overall water depth and find that the deep model can improve the correction precision by more than 17% compared with previous research. Overall, the Southern Ocean data have the highest correction precision among the three test areas, followed by the West Pacific data, and the East Pacific data ranked last.

There are many factors that contribute to the differences in accuracy of the correction. In terms of systematic errors, differences in sampling accuracy when satellites orbit at different latitudes and the band-limited correlation between gravity–altimetry signals under different geological conditions may exert an influence on the accuracy of the data [15,27]. The heterogeneous quality of the multibeam sonar data, the truth value, during ship measurements can also affect the inversion results. In addition, resampling, as a fitting process, inherently introduces errors, which may also vary with different resampling

approaches. A quantitative analysis of the error mechanism needs to be elaborated in more detail in future studies in order to promote the method globally.

The generalizability of the model can have an impact on the ability to predict new unknown data, and there is some room for enhancement if greater data size is applied. On the one hand, a new piece of bathymetric data can be considered in the validation set instead of the other half of the same bathymetric data, in order to increase the noise and add more randomness to the search for the optimal solution of the loss function. On the other hand, a comparison of different optimizer types can be included to select the one that can combine the optimal performance of the loss and generalization [34,47].

**Author Contributions:** Conceptualization, X.L. and Z.W.; data curation, X.C., J.S., M.W., H.W. and B.L.; formal analysis, X.C.; funding acquisition, X.L. and Z.W.; investigation, X.C.; methodology, X.C., X.L. and X.Q.; project administration, Z.W.; resources, X.C. and X.L.; software, X.C. and X.Q.; supervision, X.C., X.L., Z.W., J.S. and M.W.; writing—original draft, X.C.; writing—review and editing, X.C. All authors have read and agreed to the published version of the manuscript.

**Funding:** The following projects fund this research: (1) National Natural Science Foundation of China (41830540). (2) National Key Research and Development Program of China (2020YFC1521700 and 2020YFC1521705). (3) The Open Fund of the East China Coastal Field Scientific Observation and Research Station of the Ministry of Natural Resources (ORSECCZ2022104). (4) The Deep Blue Project of Shanghai Jiao Tong University (SL2020ZD204). (5) Monitoring of topographic changes and evolution of sedimentary environment in Tumen River estuary, Central-level public welfare research institutes of the basic research operating expenses of special funds for projects of China (SZ2102). (6) Zhejiang Provincial Project (330000210130313013006).

**Data Availability Statement:** The authors would like to express gratitude to the National Geophysical Data Center (NGDC) of National Oceanic and Atmospheric Administration (NOAA) for data services [45,46].

**Conflicts of Interest:** The authors declare no conflict of interest.

## References

1. Fox, C.G.; Chadwick, W.W., Jr.; Embley, R.W. Detection of changes in ridge-crest morphology using repeated multibeam sonar surveys. *J. Geophys. Res. Solid Earth* **1992**, *97*, 11149–11162. [[CrossRef](#)]
2. Wu, Y. A Study on Multi-Beam Sounding System Seafloor Tracking & Data Processing Techniques. Ph.D. Thesis, Harbin Engineering University, Harbin, China, 2001.
3. Schimel, A.C.G.; Ierodiaconou, D.; Hulands, L.; Kennedy, D.M. Accounting for uncertainty in volumes of seabed change measured with repeat multibeam sonar surveys. *Cont. Shelf Res.* **2015**, *111*, 52–68. [[CrossRef](#)]
4. Ma, J.; Jin, J.; Liu, Q. Multibeam Echosounder Versus Side Scan Object Detection: A Comparative Analysis. *Hydrograph* **2006**, *26*, 10–12. [[CrossRef](#)]
5. Ji, X. Classification of Seabed Sediment and Terrain Complexity Based on Multibeam Data. Master's Thesis, First Institute of Oceanography, Ministry of Natural Resources, Beijing, China, 2017.
6. Pike, S.; Traganos, D.; Poursanidis, D.; Williams, J.; Medcalf, K.; Reinartz, P.; Chrysoulakis, N. Leveraging Commercial High-Resolution Multispectral Satellite and Multibeam Sonar Data to Estimate Bathymetry: The Case Study of the Caribbean Sea. *Remote Sens.* **2019**, *11*, 1830. [[CrossRef](#)]
7. Cooper, I.; Hotchkiss, R.H.; Williams, G.P. Extending Multi-Beam Sonar with Structure from Motion Data of Shorelines for Complete Pool Bathymetry of Reservoirs. *Remote Sens.* **2021**, *13*, 35. [[CrossRef](#)]
8. Pydyn, A.; Popek, M.; Kubacka, M.; Janowski, Ł. Exploration and reconstruction of a medieval harbour using hydroacoustics, 3-D shallow seismic and underwater photogrammetry: A case study from Puck, southern Baltic Sea. *Archaeol. Prospect.* **2021**, *28*, 527–542. [[CrossRef](#)]
9. Li, J. *Multibeam Survey Principles, Techniques and Methods*; Ocean Press: Beijing, China, 1999.
10. Coley, K. A Global Ocean Map is Not an Ambition, but a Necessity to Support the Ocean Decade. *Mar. Technol. Soc. J.* **2022**, *56*, 9–12. [[CrossRef](#)]
11. Agrafiotis, P.; Karantzas, K.; Georgopoulos, A.; Skarlatos, D. Correcting Image Refraction: Towards Accurate Aerial Image-Based Bathymetry Mapping in Shallow Waters. *Remote Sens.* **2020**, *12*, 322. [[CrossRef](#)]
12. Liu, Y.M.; Deng, R.R.; Qin, Y.; Liang, Y.H. Data processing methods and applications of airborne LiDAR bathymetry. *J. Remote Sens.* **2017**, *21*, 982–995. [[CrossRef](#)]
13. Parker, R.L. The Rapid Calculation of Potential Anomalies. *Geophys. J. Int.* **1972**, *31*, 447–455. [[CrossRef](#)]

14. Dixon, T.H.; Naraghi, M.; McNutt, M.K.; Smith, S.M. Bathymetric prediction from Seasat altimeter data. *J. Geophys. Res. Oceans* **1983**, *88*, 1563–1571. [[CrossRef](#)]
15. Smith, W.H.F.; Sandwell, D.T. Bathymetric prediction from dense satellite altimetry and sparse shipboard bathymetry. *J. Geophys. Res. Solid Earth* **1994**, *99*, 21803–21824. [[CrossRef](#)]
16. Ramillien, G.; Cazenave, A. Global bathymetry derived from altimeter data of the ERS-1 geodetic mission. *J. Geodyn.* **1997**, *23*, 129–149. [[CrossRef](#)]
17. Arabelos, D. On The Possibility to Estimate Ocean Bottom Topography from Marine Gravity and Satellite Altimeter Data Using Collocation. In *Geodesy on the Move*; Forsberg, R., Feissel, M., Dietrich, R., Eds.; Springer: Berlin/Heidelberg, Germany, 1998; Volume 117, pp. 105–112. [[CrossRef](#)]
18. Calmant, S.; Baudry, N. Modelling bathymetry by inverting satellite altimetry data: A review. *Mar. Geophys. Res.* **1996**, *18*, 123–134. [[CrossRef](#)]
19. Yeu, Y.; Yee, J.-J.; Yun, H.S.; Kim, K.B. Evaluation of the Accuracy of Bathymetry on the Nearshore Coastlines of Western Korea from Satellite Altimetry, Multi-Beam, and Airborne Bathymetric LiDAR. *Sensors* **2018**, *18*, 2926. [[CrossRef](#)] [[PubMed](#)]
20. Brêda, J.P.L.F.; Paiva, R.C.D.; Bravo, J.M.; Passaia, O.A.; Moreira, D.M. Assimilation of Satellite Altimetry Data for Effective River Bathymetry. *Water Resour. Res.* **2019**, *55*, 7441–7463. [[CrossRef](#)]
21. Wöfl, A.-C.; Snaith, H.; Amirebrahimi, S.; Devey, C.W.; Dorschel, B.; Ferrini, V.; Huvenne, V.A.I.; Jakobsson, M.; Jencks, J.; Johnston, G.; et al. Seafloor Mapping—The Challenge of a Truly Global Ocean Bathymetry. *Front. Mar. Sci.* **2019**, *6*, 283. [[CrossRef](#)]
22. Sepúlveda, I.; Tozer, B.; Haase, J.S.; Liu, P.L.-F.; Grigoriu, M. Modeling Uncertainties of Bathymetry Predicted with Satellite Altimetry Data and Application to Tsunami Hazard Assessments. *J. Geophys. Res. Solid Earth* **2020**, *125*, 9. [[CrossRef](#)]
23. Dierssen, H.M.; Theberge, A.E. Bathymetry: Assessment. In *Coastal and Marine Environments*, 2nd ed.; CRC Press: Boca Raton, FL, USA, 2020; pp. 175–184.
24. Dettmering, D.; Ellenbeck, L.; Scherer, D.; Schwatke, C.; Niemann, C. Potential and Limitations of Satellite Altimetry Constellations for Monitoring Surface Water Storage Changes—A Case Study in the Mississippi Basin. *Remote Sens.* **2020**, *12*, 3320. [[CrossRef](#)]
25. Wu, Z.; Yang, F.; Tang, Y. *High-Resolution Seafloor Survey and Applications*; Science Press: Beijing, China, 2021.
26. Zhang, B.; Chen, Y.; Yuan, Y. PPP-RTK based on undifferenced and uncombined observations: Theoretical and practical aspects. *J. Geod.* **2019**, *93*, 1011–1024. [[CrossRef](#)]
27. Zhang, B.; Hou, P.; Zha, J.; Liu, T. Integer-estimable FDMA model as an enabler of GLONASS PPP-RTK. *J. Geod.* **2021**, *95*, 91. [[CrossRef](#)]
28. Mou, L.; Ghamisi, P.; Zhu, X.X. Deep Recurrent Neural Networks for Hyperspectral Image Classification. *IEEE Trans. Geosci. Remote Sens.* **2017**, *55*, 3639–3655. [[CrossRef](#)]
29. Li, S.; Song, W.; Fang, L.; Chen, Y.; Ghamisi, P.; Benediktsson, J.A. Deep Learning for Hyperspectral Image Classification: An Overview. *IEEE Trans. Geosci. Remote Sens.* **2019**, *57*, 6690–6709. [[CrossRef](#)]
30. Hong, D.; Gao, L.; Yao, J.; Zhang, B.; Plaza, A.; Chanussot, J. Graph Convolutional Networks for Hyperspectral Image Classification. *IEEE Trans. Geosci. Remote Sens.* **2021**, *59*, 5966–5978. [[CrossRef](#)]
31. Girshick, R.; Donahue, J.; Darrell, T.; Malik, J. Rich Feature Hierarchies for Accurate Object Detection and Semantic Segmentation. In Proceedings of the 2014 IEEE Conference on Computer Vision and Pattern Recognition, Columbus, OH, USA, 24–27 June 2014. [[CrossRef](#)]
32. Evans, M.C.; Ruf, C.S. Toward the Detection and Imaging of Ocean Microplastics with a Spaceborne Radar. *IEEE Trans. Geosci. Remote Sens.* **2022**, *60*, 4202709. [[CrossRef](#)]
33. Gatys, L.A.; Ecker, A.S.; Bethge, M. A Neural Algorithm of Artistic Style. *J. Vis.* **2015**, *16*, 326. [[CrossRef](#)]
34. Gatys, L.A.; Ecker, A.S.; Bethge, M.; Hertzmann, A.; Shechtman, E. Controlling Perceptual Factors in Neural Style Transfer. In Proceedings of the IEEE Conference on Computer Vision and Pattern Recognition, Honolulu, HI, USA, 22–25 July 2017. [[CrossRef](#)]
35. Jena, B.; Kurian, P.J.; Swain, D.; Tyagi, A.; Ravindra, R. Prediction of bathymetry from satellite altimeter based gravity in the Arabian Sea: Mapping of two unnamed deep seamounts. *Int. J. Appl. Earth Obs. Geoinf.* **2012**, *16*, 1–4. [[CrossRef](#)]
36. Jha, S.K.; Mariethoz, G.; Kelly, B.F.J. Bathymetry fusion using multiple-point geostatistics: Novelty and challenges in representing non-stationary bedforms. *Environ. Model. Softw.* **2013**, *50*, 66–76. [[CrossRef](#)]
37. Moran, N.P. Machine Learning Model Selection for Predicting Global Bathymetry. Master’s Thesis, University of New Orleans, New Orleans, LA, USA, 2020.
38. Ghorbanidehno, H.; Lee, J.; Farthing, M.; Tyler, H.; Darve, E.F.; Kitanidis, P.K. Deep learning technique for fast inference of large-scale riverine bathymetry. *Adv. Water Resour.* **2021**, *147*, 103715. [[CrossRef](#)]
39. Krizhevsky, A.; Sutskever, I.; Hinton, G.E. ImageNet Classification with Deep Convolutional Neural Networks. In Proceedings of the 25th International Conference on Neural Information Processing Systems, Lake Tahoe, NV, USA, 3–6 December 2012. [[CrossRef](#)]
40. Jia, Y.; Shelhamer, E.; Donahue, J.; Karayev, S.; Long, J.; Girshick, R.; Guadarrama, S.; Darrell, T. Caffe: Convolutional Architecture for Fast Feature Embedding. In Proceedings of the 22nd ACM International Conference, Orlando, FL, USA, 3–7 November 2014. [[CrossRef](#)]
41. Simonyan, K.; Zisserman, A. Very Deep Convolutional Networks for Large-Scale Image Recognition. In Proceedings of the 3rd International Conference on Learning Representations, San Diego, CA, USA, 7–9 May 2015.

42. Huo, G.; Wu, Z.; Li, J. Underwater Object Classification in Sidescan Sonar Images Using Deep Transfer Learning and Semisynthetic Training Data. *IEEE Access* **2020**, *8*, 47407–47418. [[CrossRef](#)]
43. Islam, M.J.; Xia, Y.; Sattar, J. Fast Underwater Image Enhancement for Improved Visual Perception. *IEEE Robot. Autom. Lett.* **2020**, *5*, 3227–3234. [[CrossRef](#)]
44. Schulz, M.-A.; Yeo, B.T.T.; Vogelstein, J.T.; Mourao-Miranada, J.; Kather, J.N.; Kording, K.; Richards, B.; Bzdok, D. Different scaling of linear models and deep learning in UKBiobank brain images versus machine-learning datasets. *Nat. Commun.* **2020**, *11*, 4238. [[CrossRef](#)] [[PubMed](#)]
45. NOAA National Centers for Environmental Information: Multibeam Bathymetry Database (MBBDB). Available online: <https://www.ncei.noaa.gov/access/metadata/landing-page/bin/iso?id=gov.noaa.ngdc:G01034> (accessed on 6 December 2021).
46. NOAA National Geophysical Data Center: ETOPO1 1 Arc-Minute Global Relief Model. Available online: <http://www.ncei.noaa.gov/access/metadata/landing-page/bin/iso?id=gov.noaa.ngdc.mgg.dem:316> (accessed on 6 December 2021).
47. Reddi, S.J.; Kale, S.; Kumar, S. On the Convergence of Adam and Beyond. In Proceedings of the 6th International Conference on Learning Representations, Vancouver, BC, Canada, 30 April–3 May 2018.